ESAIM: M2AN 60 (2026) 1247–1268
https://doi.org/10.1051/m2an/2026033

ESAIM: Mathematical Modelling and Numerical Analysis
www.esaim-m2an.org

NUMERICAL SIMULATION OF A FINE-TUNABLE FÖPPL–VON KÁRMÁN MODEL FOR FOLDABLE AND BILAYER PLATES

Sören Bartels[1,*], Bernd Schmidt[2] and Philipp Tscherner[1]

Abstract. A numerical scheme is proposed to identify low energy configurations of a Föppl–von Kármán model for bilayer plates. The dependency of the corresponding elastic energy on the in-plane displacement u and the out-of-plane deflection w leads to a practical minimization of the functional *via* a decoupled gradient flow. In particular, the energies of the resulting iterates are shown to be monotonically decreasing. The discretization of the model relies on $P1$ finite elements for the horizontal part u and utilizes the discrete Kirchhoff triangle for the vertical component w. The model allows for analysing various different problem settings *via* numerical simulation: (i) stable low-energy configurations are detected dependent on a specified prestrain described by elastic material properties, (ii) curvature inversions of spherical and cylindrical configurations are investigated, (iii) elastic responses of foldable cardboards for different spontaneous curvatures and crease geometries are compared.

Mathematics Subject Classification. 65N30, 74B20, 74K20.

Received February 24, 2025. Accepted April 4, 2026.

1. Introduction

The rigorous justification and numerical treatment of bilayer plate models have recently received considerable attention [4,6], as they give rise to a wide range of applications including heated materials with inhomogeneous expansion coefficients [30] and crystallizations on top of substrates [19,29]. Similar mechanics can be observed in natural systems, *e.g.*, in biological materials with internal misfit caused by swelling or growing tissue [17,24]. Investigating such models can provide a deeper understanding of the elastic processes involved. A well-known model to describe elastic deformations of thin objects including nonlinear effects is the Föppl–von Kármán model [9]. The authors of [10,11] recently derived such a model for bilayer plates *via* Γ-convergence, we refer to the seminal contributions [15,16] for underlying concepts. It includes a parameter $\theta > 0$ that determines the strength of prestrain acting on the elastic body. Under the assumption that the material is homogeneous with linear internal misfit, the deformation of a plate $\Omega \subset \mathbb{R}^2$ can be described by an in-plane displacement $u : \Omega \to \mathbb{R}^2$ and an out-of-plane deflection $w : \Omega \to \mathbb{R}$ *via* minimization of the dimensionally reduced elastic

---

Keywords and phrases. Nonlinear elasticity, Föppl–von Kármán model, bilayer plates, gradient flow, folding.

[1] Abteilung für angewandte Mathematik, Albert-Ludwigs-Universität Freiburg, Hermann-Herder-Str. 10, 79104 Freiburg im Breisgau, Germany.

[2] Institut für Mathematik, Universität Augsburg, Universitätsstr. 14, 86159 Augsburg, Germany.

[*]Corresponding author: `bartels@mathematik.uni-freiburg.de`

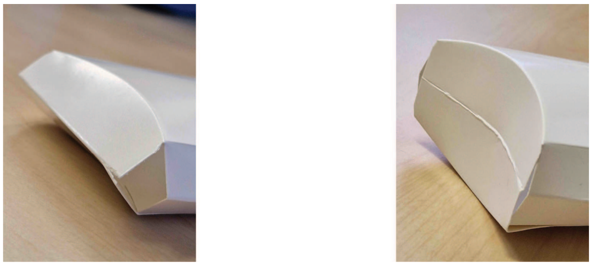

FIGURE 1. Bistable mechanism of a foldable cardboard. After repeated actuation, a crack can be observed (*left* picture) which emerges from the boundary and spreads along the given crease.

energy

$$E^\theta(u,w) = \frac{1}{2}\int_\Omega |D^2 w - \alpha I|^2 \,\mathrm{d}x + \frac{\theta}{2}\int_\Omega |\nabla w \otimes \nabla w + \widetilde{\varepsilon}(u)|^2 \,\mathrm{d}x - \int_\Omega f w \,\mathrm{d}x,$$

in a set of admissible pairs $(u,w) \in H^1(\Omega,\mathbb{R}^2) \times H^2(\Omega)$ subject to appropriate boundary conditions and a vertical dead body load $f : \Omega \to \mathbb{R}$. The first term in the energy captures bending phenomena *via* deviations of the Hessian to the identity matrix scaled by some parameter $\alpha \in \mathbb{R}$ with respect to the squared Frobenius norm $|A|^2 := \sum_{i=1}^2 \sum_{j=1}^2 |a_{ij}|^2$, thereby leading to the preference of a certain curvature in the out-of-plane deflection w. The second part of the energy includes shearing effects and involves twice the symmetric gradient $\widetilde{\varepsilon}(u) = \nabla u + \nabla u^\top$ and the dyadic product $x \otimes y = xy^\mathsf{T}$, which introduces a coupling of the in- and out-of-plane components u and w, whose strength depends on the parameter choice $\theta \in (0,\infty)$. Extending previous results which considered limiting energy functionals within regimes in which the typical energy per unit volume scales with powers of the film thickness γ (see, in particular, [16,20,21]), the parameter θ introduces an additional fine scale in the von Kármán regime γ^4. Indeed, for $\theta = 0$, E^θ reduces to the energy functional of a linear plate theory whereas, for $\theta = \infty$, the limiting energy E^θ is that of a linearized Kirchhoff plate theory in which $\nabla w \otimes \nabla w$ is constrained to be a symmetrized gradient or, equivalently (cf. [16]), w satisfies the linearized isometry constraint $\det D^2 w = 0$. Thus, the von Kármán functional augmented with the parameter θ provides a mathematical model that allows to discriminate 'thick' and 'thin' plates. In particular, it is able to mathematically sustain a basic phenomenon observed in engineering systems ([12–14, 18, 22, 25]: Large prestrains in very thin layers result in cylindrical shapes whereas small prestrains in thick layers lead to spherical caps, see [10].)

Furthermore, a piecewise minimization of the energy on two adjacent domains coupled with a continuity condition along a given connecting crease line lead to simulations of foldable single- and multilayer devices. Consequently, many interesting phenomena like the elastic response of foldable cardboards, cf. Figure 1, or the actuation of bilayer mechanisms inspired by Venus flytraps, can be numerically investigated.

The nonconvex structure of the elastic energy complicates the computation of global minimizers. An effective method to numerically detect stationary configurations with low elastic energy has been proposed in [3]. It includes a gradient flow for the energy with respect to both variables u and w. Only small modifications are required to adapt it to the energy functional under consideration. The numerical scheme is based on a discretization of the coupled system of nonlinear evolution equations

$$\begin{aligned}
\big(\partial_t w, v\big)_{\mathrm{ver}} &= -\,\partial_w E^\theta(u,w)[v] \\
&= -\,\big(D^2 w - \alpha I, D^2 v\big) - 2\theta\big(|\nabla w|^2 \nabla w + \widetilde{\varepsilon}(u)\nabla w, \nabla v\big) + \big(f, v\big), \\
\big(\partial_t u, z\big)_{\mathrm{hor}} &= -\,\partial_u E^\theta(u,w)[z] \\
&= -\,\theta\big(\widetilde{\varepsilon}(u), \widetilde{\varepsilon}(z)\big) - \theta\big(\nabla w \otimes \nabla w, \widetilde{\varepsilon}(z)\big),
\end{aligned}$$

with the Fréchet derivatives $\partial_w E^\theta$, $\partial_u E^\theta$ and inner products $(\cdot\,,\cdot)$, $(\cdot\,,\cdot)_{\rm ver}$ and $(\cdot\,,\cdot)_{\rm hor}$ on $L^2(\Omega)$, $H^2(\Omega)$ and $H^1(\Omega,\mathbb{R}^2)$, respectively. The identities $|a\otimes a|^2=|a|^4$ and $S:(a\otimes b)=(Sa)\cdot b=(Sb)\cdot a$ for symmetric matrices $S\in\mathbb{R}^{2\times 2}$ and vectors $a,b\in\mathbb{R}^2$ have been used in the derivation of the above system of equations.

To specify a discrete version of the evolution equations, time derivatives are replaced by the backward difference quotients

$$d_t u^k=\frac{1}{\tau_k}\big(u^k-u^{k-1}\big),\quad d_t w^k=\frac{1}{\tau_k}\big(w^k-w^{k-1}\big),$$

where $(\tau_k)_{k\geq 1}$ denotes a sequence of positive step sizes. A decoupling of the evolution equations is employed to combine practical stability properties of an implicit discretization with amenable solvability of an explicit treatment. In the same manner, we make use of the delay effect of the discrete product rule and define the average $w^{k-1/2}$ as

$$w^{k-1/2}=\frac{1}{2}\big(w^k+w^{k-1}\big),$$

to arrive at the following iterative scheme: Given (u^{k-1},w^{k-1}) compute (u^k,w^k) such that

$$\begin{aligned}\big(d_t w^k,v\big)_{\rm ver}&=-\,\big(D^2w^k-\alpha I,D^2v\big)-2\theta\big(|\nabla w^k|^2\nabla w^k+\widetilde{\varepsilon}(u^{k-1})\nabla w^{k-1/2},\nabla v\big)+\big(f,v\big),\\ \big(d_t u^k,z\big)_{\rm hor}&=-\,\theta\big(\widetilde{\varepsilon}(u^k),\widetilde{\varepsilon}(z)\big)-\theta\big(\nabla w^k\otimes\nabla w^k,\widetilde{\varepsilon}(z)\big),\end{aligned}$$

for all (v,z) satisfying homogeneous boundary conditions. We show that the scheme is unconditionally stable and energy decreasing which implies convergence of a sequence (u^k,w^k) to a stationary configuration (u,w). To ensure well-posedness of the equations we employ the following adaptive time stepping scheme that includes an appropriate parameter $\tau_{\max}>0$ to prevent numerical overflow:

- decrease τ_k until the Newton scheme terminates within $N>0$ iterations;
- set $\tau_{k+1}=\min\big\{2\tau_k,\tau_{\max}\big\}$ for the next gradient flow step.

The dependence of the Föppl–von Kármán model on the in-plane and out-of-plane components allows for different spatial discretizations of the two respective variables. In particular, the displacement u is discretized using P_1 finite elements whereas the deflection w is discretized *via* the discrete Kirchhoff triangle [1]. The latter allows for a practical realization of bending elements since the discrete gradient values $\nabla_h w_h$ belong to degrees of freedom of the finite element space. The discrete elastic energy functional reads

$$\begin{aligned}E_h^\theta(u_h,w_h)=&\,\frac{1}{2}\int_\Omega|\nabla\nabla_h w_h-\alpha I|^2\,{\rm d}x\\&+\frac{\theta}{2}\int_\Omega\widehat{\mathcal{I}}_h\big[|\nabla w_h\otimes\nabla w_h+\widetilde{\varepsilon}(u_h)|^2\big]\,{\rm d}x-\int_\Omega\widehat{\mathcal{I}}_h\big[fw_h\big]\,{\rm d}x,\end{aligned}$$

where $\widehat{\mathcal{I}}_h$ is the elementwise nodal interpolation operator introduced in Section 2.3 and ∇_h denotes the discrete gradient operator defined in Section 2.4. As in [3] it follows that under appropriate boundary conditions the discrete elastic energies E_h^θ are Γ-convergent to the continuous elastic energy E^θ in $H^1(\Omega,\mathbb{R}^2)\times W^{1,4}(\Omega)$ for a sequence of regular triangulations $(\mathscr{T}_h)_{h>0}$ as $h\to 0$.

The practical realization of the model based on rigorously justified numerical methods is motivated by results from [10]. The authors quantify configurations of spherical and cylindrical shape as energy minimizing configurations of the continuous limit models as $\theta\to 0$ and $\theta\to\infty$, respectively. We investigate stationary low energy configurations of the discrete model for intermediate values $\theta\in(0,\infty)$ *via* numerical experiments. The aim is to possibly identify a critical range of values θ at which a rapid transition from spherical to cylindrical shape takes place. Such a stark change of material response in a critical parameter region has been indicated by first experiments in [10], which were based on an ad-hoc projected gradient descent using nonconforming

P_1 elements on the out-of-plane strain and enforcing this quantity to be curl-free eventually by a penalization. Our present numerical analysis and implementation detailed below substantiates these observations. Moreover, we perform numerical experiments on the curvature inversion of the resulting spherical and cylindrical configurations and investigate the elastic responses of foldable cardboards for different spontaneous curvatures and crease geometries.

The outline of this article is as follows. Section 2 is devoted to the derivation of the continuous Föppl–von Kármán model along with discretization aspects. In Section 3 we show the energy decreasing property of the discrete gradient flow. The Γ-convergence of the discrete energy E_h^θ to the continuous energy E^θ is addressed in Section 4. Section 5 contains various numerical experiments.

2. Preliminaries

2.1. Model derivation

A rigorous derivation of the Föppl–von Kármán model for prestrained plates has been established in [11] *via* Γ-convergence. For a thin plate $\Omega_\gamma = \Omega \times (-\gamma/2, \gamma/2)$ of thickness $\gamma > 0$ with $\Omega \subset \mathbb{R}^2$ a bounded Lipschitz domain and some elastic energy density $W_\gamma : \mathbb{R}^{3\times 3} \to \mathbb{R}$, the corresponding three-dimensional scaled hyperelastic energy reads

$$E_{3\mathrm{d}}^{\gamma}(y) = \frac{1}{\gamma^4}\int_{\Omega_1} W_\gamma(x_3, \partial_1 y, \partial_2 y, \gamma^{-1}\partial_3 y)\,\mathrm{d}x,$$

where $y \in H^1(\Omega_1, \mathbb{R}^3)$ is defined *via* rescaling to the plate Ω_1 of thickness $\gamma = 1$. In contrast to general singlelayer models, the energy considered here explicitly depends on the out-of-plane variable $x_3 \in (-1/2, 1/2)$. The elastic energy density W_γ reads

$$W_\gamma(x_3, F) = W_0\Big(x_3, F\Big(I + \gamma^2\sqrt{\theta}B_\gamma(x_3)\Big)\Big), \quad F \in \mathbb{R}^{3\times 3},$$

and is described by the stored energy density W_0 of the reference configuration that depends on some *internal misfit* $B_\gamma : (-1/2, 1/2) \to \mathbb{R}^{3\times 3}$ weighted by $\gamma^2\sqrt{\theta}$ with a parameter $\theta \in (0, \infty)$. The energy density W_0 is assumed to satisfy the classical, physically motivated requirements such as *smoothness* in a neighbourhood of $SO(3)$, *frame indifference*, *non-degeneracy*, and *quadratic growth*, so that it is minimal (with value 0) precisely on $SO(3)$. As the strength of the misfit scales with γ^2, typical deformation gradients deviate from $SO(3)$ by a comparable amount and the effect of the prestrain is suitably described within the von Kármán energy scaling γ^4. More precisely, the strength of the misfit is $\sqrt{\theta}\gamma^2$, so that the variable θ specifies the amount of misfit on the scale γ^2 and serves as an interpolation between the linearized von Kármán ($\theta \to 0$) and the linearized Kirchhoff ($\theta \to \infty$) models as $\gamma \to 0$. By frame invariance of the three dimensional energy density W_0, rigid body motions do not store elastic energy so that for each deformation y and $R \in SO(3)$, $c \in \mathbb{R}^3$ one has

$$E_{3\mathrm{d}}^{\gamma}(y) = E_{3\mathrm{d}}^{\gamma}(Ry + c).$$

Considering the asymptotic behavior of a sequence of rescaled deformations as $\gamma \to 0$ we may and will thus renormalize by tacitly applying a rigid body motion to the plate so as to guarantee that

$$\|y - \mathrm{id}_\gamma\|_{L^2} = \min\big\{\|Ry + c - \mathrm{id}_\gamma\| : R \in SO(3),\, c \in \mathbb{R}^3\big\}, \tag{2.1}$$

where $\mathrm{id}_\gamma(x) = (x_1, x_2, \gamma x_3)$. In the von Kármán regime one then considers the rescaled in-plane and out-of-plane displacements

$$\widehat{u}_i(x) = \frac{1}{\theta\gamma^2}(y_i(x) - x_i) \quad (i = 1, 2) \quad \text{and} \quad \widehat{w}(x) = \frac{1}{\sqrt{\theta}\gamma}y_3(x) \tag{2.2}$$

and their averages along the small plate height

$$u_i(x_1,x_2)=\int_{-1/2}^{1/2}\widehat{u}_i(x)\,\mathrm{d}x_3\quad(i=1,2)\quad\text{and}\quad w(x_1,x_2)=\int_{-1/2}^{1/2}\widehat{w}(x)\,\mathrm{d}x_3$$

as $\gamma\to 0$. The Γ-limit of $E^{\gamma}_{3\mathrm{d}}$ together with a suitable compactness results for bounded energy sequences has been obtained in [11] with respect to convergence of the averaged displacement variable (u,w). Since the corresponding deformation gradients are close to rotations, the resulting energy functional $(u,w)\mapsto E^{\theta}(u,w)$ only depends on the infinitesimal elastic moduli and is explicitly computable from $D^2_F W_0(t,I)$. Omitting the forcing term, for the prototypical example of an isotropic homogeneous material with $W_0(t,F)=\operatorname{dist}^2(F,SO(3))$ and linear internal misfit $B(t)=\alpha t I$ we arrive at the following energy functional

$$E^{\theta}(u,w)=\frac{1}{2}\int_{\Omega}|D^2w-\alpha I|^2\,\mathrm{d}x+\frac{\theta}{2}\int_{\Omega}|\nabla w\otimes\nabla w+\widetilde{\varepsilon}(u)|^2\,\mathrm{d}x,$$

which is a rescaled version of the general Föppl–von Kármán functional. The corresponding set of admissible pairs $(u,w)\in\mathcal{A}$ is defined as

$$\mathcal{A}=\mathcal{A}_0+(u_D,w_D)\subset H^1(\Omega,\mathbb{R}^2)\times H^2(\Omega).$$

Here, $\mathcal{A}$ and $\mathcal{A}_0$ are affine and linear subspaces of $H^1(\Omega,\mathbb{R}^2)\times H^2(\Omega)$, respectively, such that the following Korn–Poincaré inequality holds, *i.e.*,

$$||u_0||_{H^1(\Omega;\mathbb{R}^2)}+||w_0||_{H^2(\Omega)}\le c_P\Big(||\widetilde{\varepsilon}(u_0)||+||D^2w_0||\Big) \tag{2.3}$$

for all $(u_0,w_0)\in\mathcal{A}_0$. For instance, this is the case if we have

$$u_0|_{\gamma_D}=0,\quad w_0|_{\gamma_D}=0,\quad \nabla w_0|_{\gamma_D}=0,$$

on a subset $\gamma_D\subset\partial\Omega$ of positive surface measure or

$$u_0|_{\partial\Omega}=0,\quad w_0|_{\partial\Omega}=0,$$

on the whole boundary $\partial\Omega$ of Ω. To guarantee well-posedness of the iterative scheme, we note that the Sobolev inequality

$$||\nabla w_0||_{L^4(\Omega)}\le c_S||D^2w_0|| \tag{2.4}$$

holds for all $w_0\in\mathcal{A}_0$ due to the Sobolev embedding $H^2(\Omega)\hookrightarrow W^{1,4}(\Omega)$.

Our results on the minimizers of E^{θ} yields a very precise asymptotic analysis of low energy configurations for the original three dimensional functional, which for definiteness we formulate here for the prototypical case

$$E^{\gamma}_{3\mathrm{d}}(y)=\frac{12}{\gamma^4}\int_{\Omega_1}\operatorname{dist}^2\Big(\Big(1+\gamma^2(\theta/3)^{1/2}\,x_3\Big)\big(\partial_1y,\partial_2y,\gamma^{-1}\partial_3y\big),SO(3)\Big)\,\mathrm{d}x.$$

(We introduced irrelevant constants so as to arrive at the simplest limiting functional.)

A first consequence of the Γ-convergence of $E^{\gamma}_{3\mathrm{d}}$ to E^{θ} is that for a sequence of (almost) minimizers y_γ of $E^{\gamma}_{3\mathrm{d}}$ one has subsequential convergence of the rescaled averaged dispacements $u_\gamma\to u$ and $w_\gamma\to w$, where (u,w) is a minimizer of E^{θ}. Indeed, combining the Γ-convergence and compactness results in Theorem 3.1 and Lemma 4.1 from [11] with the observation in Proposition 2 from [8] yields a slightly stronger result for the limiting behavior of the full displacements in (2.2) with limiting plate functional

$$E^{\theta}(u,w)=\frac{1}{2}\int_{\Omega}|D^2w-\alpha I|^2\,\mathrm{d}x+\frac{\theta}{2}\int_{\Omega}|\nabla w\otimes\nabla w+\widetilde{\varepsilon}(u)|^2\,\mathrm{d}x.$$

Theorem 2.1. *Suppose* $(y_\gamma) \subset H^1(\Omega_1,\mathbb{R}^3)$ *is a sequence of almost minimizers for* $E^\gamma_{3\mathrm{d}}$*, i.e.,*

$$\lim_{\gamma\to 0}\big(E^\gamma_{3\mathrm{d}}(y_\gamma) - \min\big\{E^\gamma_{3\mathrm{d}}(y) : y \in H^1(\Omega_1,\mathbb{R}^3)\big\}\big) = 0,$$

such that (2.1) *is satisfied for every* y_γ*. Then there exists a subsequence (not relabeled) such that the corresponding displacements* $(\widehat{u}_\gamma, \widehat{w}_\gamma)$ *given in* (2.2) *satisfy*

$$\widehat{u}_\gamma \rightharpoonup \widehat{u} \text{ in } H^1\big(\Omega_1,\mathbb{R}^2\big) \quad \text{and} \quad \widehat{w}_\gamma \rightharpoonup \widehat{w} \text{ in } H^1(\Omega_1),$$

where the limiting $(\widehat{u},\widehat{w})$ *is given by*

$$\widehat{u}(x) = u(x_1,x_2) - \frac{1}{\sqrt{\theta}}x_3\big(\partial_1 w(x_1,x_2), \partial_2 w(x_1,x_2)\big),$$
$$\widehat{w}(x) = w(x_1,x_2) + \frac{1}{\sqrt{\theta}}x_3$$

and (u,w) *is a minimizer of* E^θ*.*

We note that the in-plane scale $\theta\gamma^2$ is negligible with respect to the deflection scale $\sqrt{\theta}\gamma$. Thus, the descaled original displacement is to leading order determined by the limiting deflection w:

$$\begin{aligned} y_\gamma(x) &= \Big(x_1 + \theta\gamma^2\widehat{u}_1(x) + o(\gamma^2), x_2 + \theta\gamma^2\widehat{u}_2(x) + o(\gamma^2), \sqrt{\theta}\gamma\widehat{w}(x) + o(\gamma)\Big) \\ &= (x_1,x_2,\gamma x_3) + \sqrt{\theta}\gamma\, w(x_1,x_2)(0,0,1)^\mathsf{T} + o(\gamma). \end{aligned} \tag{2.5}$$

More precisely, in terms of the scaled identity $\mathrm{id}_\gamma(x) = (x_1,x_2,\gamma x_3)$ we have:

Corollary 2.1. *Suppose* $(y_\gamma) \subset H^1(\Omega_1,\mathbb{R}^3)$ *is a sequence of almost minimizers for* $E^\gamma_{3\mathrm{d}}$ *such that* (2.1) *is satisfied for every* y_γ*. Then for a subsequence (not relabeled) we have*

$$\frac{1}{\sqrt{\theta}\gamma}(y_\gamma - \mathrm{id}_\gamma) \rightharpoonup w\,(0,0,1)^\mathsf{T} \text{ in } H^1(\Omega_1,\mathbb{R}^3),$$

where $w \in H^1(\Omega)$ *is such that* (u,w) *is a minimizer of* E^θ *for a suitable* u*, i.e., a minimizer for* $\min\{E^\theta(u,\cdot) : u \in H^1(\Omega,\mathbb{R}^2)\}$*.*

2.2. Remarks on plates with folds

While the above results apply to elastic plates, in Sections 5.4 and 5.5 below we will also report on numerical experiments for plates which can be folded along some special curves. From an analytical point of view, the derivation of suitable effective plate theories for such foldable plates is rather challenging. We include here a short discussion of the difficulties that occur when modeling infinitesimal deflections in foldable thin structures.

For homogeneous Kirchhoff plates which are subject to finite (nonlinear) bending and whose energy scales like γ^2, folds and even cracks and voids have been sucessfully analyzed in [5,26]. Following the approach in [5] one may consider a plate whose stored energy function is weakened in a tubular neighborhood of some crease line. More precisely, let $\Sigma \subset \Omega$ be a Jordan arc with both endpoints on the same connected component of $\partial\Omega$ and such that the two connected components of $\Omega \setminus \Sigma$ are themselves Lipschitz domains. Let $\Sigma_r = \{x \in \mathbb{R}^2 : \mathrm{dist}(x,\Sigma) < r\}$ and introduce the damage indicator $f^\gamma : \Omega_1 \to [0,1]$ by

$$f^\gamma(x) = \varepsilon_\gamma \chi_{\Sigma_\gamma}(x_1,x_2) + 1 - \chi_{\Sigma_\gamma}(x_1,x_2), \quad \text{where } \gamma^2 \lesssim \varepsilon_\gamma \ll \gamma.$$

(More general models can be considered.) The main result of [5] implies that, as $\gamma \to 0$ the prototypical energy functionals

$$y \mapsto \frac{1}{\gamma^2}\int_{\Omega_1} f^\gamma\, \mathrm{dist}^2\big((\partial_1 y, \partial_2 y, \gamma^{-1}\partial_3 y), SO(3)\big)\,\mathrm{d}x,$$

Γ-converge to the limiting functional

$$E_K^{\mathrm{hom}}(y) = \begin{cases} \frac{1}{24}\int_{\Omega\setminus\Sigma} |A|^2 \, \mathrm{d}x & \text{if } y \in \mathcal{A}, \\ +\infty & \text{otherwise.} \end{cases}$$

Here the admissible class $\mathcal{A}$ consists of piecewise isometric immersions:

$$\mathcal{A} = \left\{ y \in H^1(\Omega;\mathbb{R}^3) \cap H^2(\Omega\setminus\Sigma;\mathbb{R}^3) : \nabla y^{\mathsf{T}}\nabla y = I \text{ a.e. on } \Omega \right\},$$

and A is the second fundamental form of the surface $y(\Omega)$. A straightforward combination of these results with the analysis of multilayer Kirchhoff plates, cf. [23, 27, 28], then shows that the functionals

$$y \mapsto \frac{1}{\gamma^2}\int_{\Omega_1} f^\gamma \operatorname{dist}^2\big((1+\gamma(a+o_\gamma(1))\, x_3)(\partial_1 y, \partial_2 y, \gamma^{-1}\partial_3 y), SO(3)\big) \, \mathrm{d}x$$

for given $a \in \mathbb{R}$ Γ-converge to

$$E_K(y) = \begin{cases} \frac{1}{24}\int_{\Omega\setminus\Sigma} |A - aI|^2 \, \mathrm{d}x & \text{if } y \in \mathcal{A}, \\ +\infty & \text{otherwise.} \end{cases}$$

Moreover, bounded energy sequences are precompact. We remark that the scaling assumption $\gamma^2 \lesssim \varepsilon_\gamma \ll \gamma$ for the degradation strength guarantees that near the crease the material is so weak that arbitrarily large folding angles are possible at zero energy while still being strong enough not to break.

In the von Kármán regime, the interplay of possible folding angles and their energetic costs is more complicated. One natural choice is to consider a very weak regime where the damage indicator now satsifies

$$f^\gamma = \varepsilon_\gamma \chi_{\Sigma_\gamma} + 1 - \chi_{\Sigma_\gamma} \quad \text{with } \gamma^4 \lesssim \varepsilon_\gamma \ll \gamma^3.$$

Then still arbitrarily large folding angles are possible at zero energy. If we adapt the energy functional of the previous section by setting

$$E_{\mathrm{3d}}^\gamma(y) = \frac{12}{\gamma^4}\int_{\Omega_1} f^\gamma \operatorname{dist}^2\Big(\Big(1+\gamma^2(\theta/3)^{1/2}\, x_3\Big)(\partial_1 y, \partial_2 y, \gamma^{-1}\partial_3 y), SO(3)\Big) \, \mathrm{d}x,$$

we can apply the above results for Kirchhoff plates (with $a = 0$) to the functionals $\gamma^2 E_{\mathrm{3d}}^\gamma$ to see that any sequence (y_γ) with $E_{\mathrm{3d}}^\gamma(y_\gamma) \le C$ and hence $\gamma^2 E_{\mathrm{3d}}^\gamma(y_\gamma) \to 0$ converges – up to subsequences – to a limiting deformation y whose second fundamental form vanishes on the two components Ω_1, Ω_2 of $\Omega\setminus\Sigma$. But then y is a rigid motion on these sets, so there are $R_1, R_2 \in SO(3)$ and $c_1, c_2 \in \mathbb{R}^3$ such that

$$y(x) = \begin{cases} R_1 x + c_1 & \text{if } x \in \Omega_1, \\ R_2 x + c_2 & \text{if } x \in \Omega_2. \end{cases} \tag{2.6}$$

Moreover, as $y \in H^1(\Omega, \mathbb{R}^3)$ cannot jump along Σ, R_1 and R_2 are rank-1-connected and Σ must be a straight line unless $R_1 = R_2$ and $c_1 = c_2$ in which cases there is no fold at all. If $R_1 \ne R_2$ with $R_2 - R_1 = a \otimes n$, then n is a normal to Σ.

With these observations one is led to consider renormalizations by substracting from y_γ limiting deformations of the form (2.6) rather than a single rigid motion as in (2.1). Since there is no energy cost caused by the crease, the problem completely decouples and one can apply the results above on both components separately. After descaling (cf. (2.5) in the homogenous case) we see that deformations y_γ are to leading order of the form

$$y_\gamma(x) = R_i\Big((x_1, x_2, \gamma x_3) + \sqrt{\theta}\gamma\, w(x_1, x_2)(0,0,1)^{\mathsf{T}}\Big) + c_i + o(\gamma) \quad \text{for } x \in \Omega_i, \ i = 1, 2.$$

In particular, there is no energetical coupling between $w|_{\Omega_1}$ and $w|_{\Omega_2}$.

Other natural scaling regimes for the damage parameter are obtained by choosing larger values for ε_γ such as in the bending regime above, *i.e.*, $\gamma^2 \lesssim \varepsilon_\gamma \ll \gamma$. While we expect that a Γ-convergence result can be proved under the assumption that there is a unique rigid body motion as in (2.1) such that the rescaled relative in-plane and out-of-plane displacements (2.2) are convergent, we must observe now that such an assumption cannot be inferred from energy bounds. Indeed, exploratory computations indicate that if $R_i \in SO(3)$ and $c_i \in \mathbb{R}^3$ are optimal choices in (2.1) on Ω_i $i = 1, 2$, for $y = y_\gamma$, a bounded energy sequence, then

$$|R_2 - R_1|^2 \lesssim \varepsilon_\gamma^{-1}\gamma^3$$

and that configuartions with a folding angle scaling with $\varepsilon_\gamma^{-1/2}\gamma^{3/2}$ are possible but will lead to an extra 'folding energy' contribution in the limit. A full analysis of this regime appears challenging and is beyond the scope of this contribution.

2.3. P_1-finite elements

In this section we introduce the finite element space used for the discretization of the in-plane component u. For a regular triangulation $\mathscr{T}_h$ of the polygonal domain $\Omega \subset \mathbb{R}^2$, the standard P_1 finite element space is defined as

$$\mathcal{S}^1(\mathscr{T}_h) = \left\{ v_h \in C(\overline{\Omega}) \;\middle|\; v_h|_T \text{ affine for all } T \in \mathscr{T}_h \right\}.$$

If $\mathscr{N}_h$ denotes the set of nodes of the triangulation, the nodal basis functions $(\varphi_z)_{z \in \mathscr{N}_h}$ associated with $\mathcal{S}^1(\mathscr{T}_h)$ satisfy the Kronecker delta property $\varphi_z(y) = \delta_{zy}$ for all $z, y \in \mathscr{N}_h$. We introduce the space of discontinuous P_1 functions which is defined as

$$\widehat{\mathcal{S}}^1(\mathscr{T}_h) = \left\{ v_h \in L^\infty(\Omega) \;\middle|\; v_h|_T \text{ affine for all } T \in \mathscr{T}_h \right\},$$

along with the elementwise nodal interpolant $\widehat{\mathcal{I}}_h v \in \widehat{\mathcal{S}}^1(\mathscr{T}_h)$ of piecewise continuous functions $v \in L^\infty(\Omega)$ to account for gradient jumps of discrete functions across element sides $S \in \mathscr{S}_h$. In particular, if $\varphi_z^T \in L^\infty(\Omega)$ is the discontinuous function such that $\varphi_z^T(x) = \chi_T(x)\varphi_z(x)$ for all $x \in \Omega$, we define

$$\widehat{\mathcal{I}}_h v = \sum_{T \in \mathscr{T}_h} \sum_{z \in \mathscr{N}_h \cap T} v|_T(z)\varphi_z^T.$$

The interpolator is used to approximate the L^2 inner product of piecewise continuous functions or vector fields $v, w \in L^\infty(\overline{\Omega}, \mathbb{R}^\ell)$ for $\ell = 1, 2$ and coefficients $\beta_z^T = \int_T \varphi_z \,\mathrm{d}x$ *via*

$$\big(v, w\big)_h = \int_\Omega \widehat{\mathcal{I}}_h\big[v \cdot w\big] \,\mathrm{d}x = \sum_{T \in \mathscr{T}_h} \sum_{z \in \mathscr{N}_h \cap T} \beta_z^T v|_T(z) \cdot w|_T(z). \tag{2.7}$$

Furthermore, we denote by $V_h = \mathcal{S}^1(\mathscr{T}_h) \times \mathcal{S}^1(\mathscr{T}_h)$ the set of continuous P_1 vector fields.

2.4. Discrete Kirchhoff elements

To approximate the vertical component w of the Föppl–von Kármán model we employ an H^2-nonconforming finite element discretization. For a given regular triangulation $\mathscr{T}_h$ of Ω the H^1-conforming finite element spaces $W_h \subseteq H^1(\Omega)$ and $\Theta_h \subseteq H^1(\Omega, \mathbb{R}^2)$ are defined as

$$W_h := \left\{ w_h \in C(\overline{\Omega}) \;\middle|\; w_h|_T \in P_3^{\mathrm{red}}(T) \;\; \forall T \in \mathscr{T}_h,\, \nabla w_h \text{ is continuous at all } z \in \mathscr{N}_h \right\},$$

$$\Theta_h := \left\{ \theta_h \in C(\overline{\Omega}, \mathbb{R}^2) \;\middle|\; \theta_h|_T \in P_2(T)^2 \;\; \forall T \in \mathscr{T}_h \right\}.$$

The space $P_k(T)$ denotes the set of polynomials with total degree smaller than or equal to $k \geq 0$ restricted to the element $T \in \mathscr{T}_h$. Furthermore, in the definition of

$$P_3^{\text{red}}(T) := \left\{ p \in P_3(T) \,\middle|\, p(x_T) = \frac{1}{3} \sum_{z \in \mathscr{N}_h \cap T} \big(p(z) + \nabla p(z) \cdot (x_T - z)\big) \right\},$$

the degree of freedom in the center of mass $x_T = (1/3) \sum_{z \in \mathscr{N}_h \cap T} z$ of the triangle T is eliminated. The remaining degrees of freedom of the space W_h are given by the function values and the two partial derivatives at each vertex of the elements $T \in \mathscr{T}_h$. This property is especially useful for the practical realization of the discrete model.

To relate the finite element spaces W_h and Θ_h we introduce the operator $\nabla_h : W_h \to \Theta_h$ which defines a discretization of the deformation gradient. The property $\nabla_h w_h \in \Theta_h \subseteq H^1(\Omega, \mathbb{R}^2)$ for functions $w_h \in W_h$ ensures that second order derivatives can be discretized *via* the operation $\nabla\nabla_h w_h$. We let $\mathscr{S}_h$ denote the set of element sides.

Definition 2.1 (See [2], Def. 8.6)**.** For every $w_h \in W_h$ the *discrete gradient operator* $\nabla_h : W_h \to \Theta_h$ is the uniquely defined function $\theta_h = \nabla_h w_h$ such that

$$\begin{aligned} \theta_h(z) &= \nabla w_h(z) && \forall z \in \mathscr{N}_h, \\ \theta_h(z_S) \cdot n_S &= \frac{1}{2} \left(\nabla w_h(z_S^1) + \nabla w_h(z_S^2)\right) \cdot n_S && \forall S \in \mathscr{S}_h, \\ \theta_h(z_S) \cdot t_S &= \nabla w_h(z_S) \cdot t_S && \forall S \in \mathscr{S}_h. \end{aligned}$$

For every side $S \in \mathscr{S}_h$ we denote by $z_S^1, z_S^2 \in \mathscr{N}_h$ its endpoints, by $z_S = (z_S^1 + z_S^2)/2$ its midpoint and by $n_S, t_S \in \mathbb{R}^2$ the orthonormal vectors such that n_S is normal to S.

The discrete gradient operator possesses several useful interpolation properties for which we refer the reader to [2, 7]. Throughout the following we let W denote the space of deflections in $H^2(\Omega)$ satisfying homogeneous clamped or simple support boundary conditions. Moreover, the space $W_{0,h}^{\text{clamped}} \subset W_h$ contains functions w_h with $w_h|_{\gamma_D} = 0$ and $\nabla w_h|_{\gamma_D} = 0$ while functions in $W_{0,h}^{\text{simple}}$ satisfy $\widetilde{w}_h|_{\partial\Omega} = 0$.

3. ENERGY DECREASING ITERATION

This section deals with the analysis of the discrete gradient flow with regard to well-posedness, unconditional stability and monotone energy decay of the resulting iterates.

Algorithm 3.1 (Decoupled gradient flow)**.** Specify an initial configuration $(u^0, w^0) \in \mathcal{A}$, an initial step size $\tau_1 > 0$, a stopping tolerance $\varepsilon_{\text{stop}} > 0$ and set $k = 1$.

(1) Compute $(u^k, w^k) \in \mathcal{A}$ such that

$$\begin{aligned} \big(d_t w^k, v\big)_{\text{ver}} &= -\big(D^2 w^k - \alpha I, D^2 v\big) - 2\theta\Big(|\nabla w^k|^2 \nabla w^k + \widetilde{\varepsilon}\big(u^{k-1}\big)\nabla w^{k-1/2}, \nabla v\Big) + (f, v), \\ \big(d_t u^k, z\big)_{\text{hor}} &= -\theta\big(\widetilde{\varepsilon}(u^k), \widetilde{\varepsilon}(z)\big) - \theta\big(\nabla w^k \otimes \nabla w^k, \widetilde{\varepsilon}(z)\big), \end{aligned}$$

for all $(z, v) \in \mathcal{A}_0$.

(2) Terminate the algorithm if $||d_t u^k||_{\text{hor}} + ||d_t w^k||_{\text{ver}} \leq \varepsilon_{\text{stop}} \min\{1, \tau_k\}$. Otherwise, update τ_{k+1}, set $k \to k+1$ and continue with Step (1).

The algorithm admits a sequence $(u^k, w^k)_{k\geq 0} \subset \mathcal{A}$ that decreases the elastic energy. For simplicity we assume from now on that $f = 0$.

Lemma 3.1 (Energy decay)**.** *Iterates $(u^k, w^k)_{k\geq 0} \subset \mathcal{A}$ of Algorithm 3.1 satisfy*

$$E^\theta(u^K, w^K) + \sum_{k=1}^{K} \tau_k \Big(||d_t w^k||_{\mathrm{ver}}^2 + ||d_t u^k||_{\mathrm{hor}}^2 \Big) \leq E^\theta(u^0, w^0).$$

This implies that the updates $d_t u^k$ and $d_t w^k$ vanish as $k \to \infty$. Cluster points of the sequence (u^k, w^k) thus become stationary configurations for the elastic energy E^θ.

Proof. The proof follows from testing the first and second equation of the iterative scheme of Algorithm 3.1 with $v = d_t w^k$ and $z = d_t u^k$, respectively, as in [3]. ☐

The iteration is unconditionally stable, but chosing large step sizes might lead to non-uniqueness of solutions. A mild condition on τ_k ensures well-posedness of Algorithm 3.1.

Proposition 3.1 (Uniqueness of minimizers)**.** *The iterates $(u^k, w^k)_{k\geq 1} \subset \mathcal{A}$ of Algorithm 3.1 are unique, provided that $||D^2 w|| \leq c_{\mathrm{eq}} ||w||_{\mathrm{ver}}$ for deflections $w \in W$ and*

$$\tau_k \leq \frac{1}{2 c_0 c_{\mathrm{eq}}^2 c_S^2}$$

for every $k \geq 1$ with a constant c_0 depening on θ, c_S, w_D and $E_0 = E^\theta(u_0, w_0)$.

Proof. The linear equation defining u^k admits a unique solution by the Lax–Milgram lemma. The nonlinear equation with respect to w^k defines an optimality condition for the minimization problem $\min G(w)$ in the set of functions $w \in H^2(\Omega)$ satisfying homogeneous boundary conditions, where the functional G is defined as

$$\begin{aligned} G(w) = \frac{1}{2\tau_k} ||w - w^{k-1}||_{\mathrm{ver}}^2 + \frac{1}{2} ||D^2 w - \alpha I||^2 + \frac{\theta}{2} \int_\Omega |\nabla w|^4 \,\mathrm{d}x \\ + \frac{\theta}{2} \int_\Omega \widetilde{\varepsilon}(u^{k-1}) : \big[\nabla (w + w^{k-1}) \otimes \nabla (w + w^{k-1}) \big] \,\mathrm{d}x. \end{aligned}$$

The existence of a minimizer w^k follows by lower semicontinuity and coercivity on $H^2(\Omega)$. Lemma 3.1 implies that $\theta ||\widetilde{\varepsilon}(u^k) + \nabla w^k \otimes \nabla w^k||^2 \leq 2E^\theta(u^k, w^k) \leq 2E_0$. We show that $||\widetilde{\varepsilon}(u^k)|| \leq c_0$ with a constant c_0 defined below. Adding and subtracting $\nabla w^k \otimes \nabla w^k$ and ∇w_D, the Sobolev inequality (2.4) and the formula $(x+y)^2 \leq 2x^2 + 2y^2$ yield

$$\begin{aligned} ||\widetilde{\varepsilon}(u^k)|| &\leq ||\widetilde{\varepsilon}(u^k) + \nabla w^k \otimes \nabla w^k|| + ||\nabla w^k||_{L^4(\Omega)}^2 \\ &\leq \sqrt{2E_0/\theta} + 2||\nabla (w^k - w_D)||_{L^4(\Omega)}^2 + 2||\nabla w_D||_{L^4(\Omega)}^2 \\ &\leq \sqrt{2E_0/\theta} + 2c_S^2 \big(||D^2 w^k - \alpha I|| + \|\alpha I - D^2 w_D)|| \big)^2 + 2||\nabla w_D||_{L^4(\Omega)}^2 \leq c_0. \end{aligned}$$

Due to the above estimate we find with similar arguments and the Hölder inequality that

$$\begin{aligned} \frac{\theta}{2} \int_\Omega \widetilde{\varepsilon}(u^{k-1}) : \nabla w \otimes \nabla w \,\mathrm{d}x &\geq -\frac{\theta}{2} ||\widetilde{\varepsilon}(u^{k-1})|| \, ||\nabla w||_{L^4(\Omega)}^2 \\ &\geq -||\widetilde{\varepsilon}(u^{k-1})|| \, ||\nabla (w - w^{k-1})||_{L^4(\Omega)}^2 - ||\widetilde{\varepsilon}(u^{k-1})|| \, ||\nabla w^{k-1}||_{L^4(\Omega)}^2 \\ &\geq -c_0 c_S^2 ||D^2 (w - w^{k-1})||^2 - c_0 ||\nabla w^{k-1}||_{L^4(\Omega)}^2. \end{aligned}$$

The second term on the right-hand side is independent of w whereas the first term can be absorbed using $||D^2 \cdot || \leq c_{eq} || \cdot ||_{\mathrm{ver}}$, provided that $\tau_k \leq 1/(2 c_0 c_{eq}^2 c_S^2)$. In particular, the functional G is strongly convex which shows the uniqueness of the minimizer w^k. ☐

To deal with the nonlinear system of equations in Algorithm 3.1 we employ a Newton scheme. In the following we assume for simplicity that $||\cdot||_{\text{ver}} = ||D^2\cdot||$.

Proposition 3.2 (Newton scheme)**.** *Solving the first equation of Algorithm 3.1 is equivalent to seeking* $w^k \in W$ *such that* $F_k(w^k)[v] = 0$ *for all* $v \in W$ *with*

$$\begin{aligned} F_k(w)[v] = &\big(D^2[w - w^{k-1}], D^2v\big) + \tau_k\big(D^2w - \alpha I, D^2v\big) \\ &+ \tau_k\theta\big(\big[2|\nabla w|^2 + \widetilde{\varepsilon}(u^{k-1})\big]\nabla w + \widetilde{\varepsilon}(u^{k-1})\nabla w^{k-1}, \nabla v\big). \end{aligned}$$

The Newton scheme converges quadratically for sufficiently small step sizes.

4. Γ-CONVERGENCE

The validity of the discrete approximation of the dimensionally reduced elastic energy for the singlelayer model has been rigorously justified in [3] by means of Γ-convergence. The arguments developed there carry over verbatimly to the functional considered here and we briefly review the main ingredients. We omit dealing with the forcing term whose convergence analysis is standard and recap that the discrete energy reads

$$E_h^\theta(u_h, w_h) = \frac{1}{2}\int_\Omega |\nabla\nabla_h w_h - \alpha I|^2 \,\mathrm{d}x + \frac{\theta}{2}\int_\Omega \widehat{\mathcal{I}}_h\big[|\nabla w_h \otimes \nabla w_h + \widetilde{\varepsilon}(u_h)|^2\big]\,\mathrm{d}x$$

for functions $(u_h, w_h) \in V_h \times W_h$. The considered boundary conditions imply that $w_h \to ||\nabla\nabla_h w_h||$ defines a norm and that the discrete energy functionals satisfy a compactness result, cf. [3]. which ensures Γ-convergence of the discrete energy functionals E_h^θ to the continuous energy E^θ as $h \to 0$.

Theorem 4.1 (Γ-convergence, [3])**.**

(i) *Let* $(u_h, w_h)_{h>0} \subset V_h \times W_h$ *be a sequence of functions with bounded energy, i.e.,* $E_h^\theta(u_h, w_h) \le c_E$ *for all* $h > 0$*. Then there exists a pair* $(u, w) \in H^1(\Omega;\mathbb{R}^2) \times W^{1,4}(\Omega)$ *with* $w \in H^2(\Omega)$ *and a subsequence (not relabeled) such that*

$$(u_h, w_h) \to (u, w) \text{ in } H^1(\Omega;\mathbb{R}^2) \times W^{1,4}(\Omega)$$

as $h \to 0$ *and*

$$E^\theta(u, w) \le \liminf_{h\to 0} E_h^\theta(u_h, w_h).$$

(ii) *For every* $(u, w) \in H^1(\Omega;\mathbb{R}^2) \times H^2(\Omega)$ *there exists a recovery sequence* $(u_h, w_h)_{h>0} \subset V_h \times W_h$ *such that*

$$(u_h, w_h) \to (u, w) \text{ in } H^1(\Omega;\mathbb{R}^2) \times W^{1,4}(\Omega)$$

as $h \to 0$ *and*

$$\lim_{h\to 0} E_h^\theta(u_h, w_h) = E^\theta(u, w).$$

5. NUMERICAL EXPERIMENTS

5.1. Implementation

In this section we introduce the discrete version of the proposed gradient flow and analyse the performance of the corresponding MATLAB implementation. If $D_h^2 = \nabla\nabla_h$ denotes the discrete Hessian, the iterative scheme is defined *via* inner products

$$(w_h, v_h)_{\text{ver}} = \big(D_h^2 w_h, D_h^2 v_h\big), \quad (u_h, z_h)_{\text{hor}} = \big(\widetilde{\varepsilon}(u_h), \widetilde{\varepsilon}(z_h)\big)$$

for discrete functions $w_h, v_h \in W_h$ and $u_h, z_h \in V_h$. For approximations $u_{D,h} \in V_h$ and $w_{D,h} \in W_h$ of some boundary data, we define the discrete set of admissible functions as

$$\mathcal{A}_h = \mathcal{A}_{0,h} + (u_{D,h}, w_{D,h}),$$

where $\mathcal{A}_{0,h} = V_{0,h} \times W_{0,h}$ is a linear subspace subject to homogeneous boundary conditions. This leads to the following scheme for the discrete decoupled gradient flow.

Algorithm 5.1 (Discrete decoupled gradient flow)**.** Specify an initial configuration $(u_h^0, w_h^0) \in \mathcal{A}_h$, an initial step size $\tau_1 > 0$, stopping tolerances $\varepsilon_{\text{Newton}}, \varepsilon_{\text{stop}} > 0$ and set $k = 1$.

(1a) Decrease τ_k until the Newton scheme computes $w_h^k \in [W_{0,h} + w_{D,h}]$ within a tolerance $||D_h^2 d_t w_h^k|| \le \varepsilon_{\text{Newton}}$ and a maximum number $N > 0$ of iterations such that

$$\begin{aligned}\big(D_h^2 d_t w_h^k, D_h^2 v_h\big) = &-\big(D_h^2 w_h^k - \alpha I, D_h^2 v_h\big)\\ &- 2\theta\Big(\big|\nabla w_h^k\big|^2 \nabla w_h^k + \widetilde{\varepsilon}\big(u_h^{k-1}\big)\nabla w_h^{k-1/2}, \nabla v_h\Big)_h + \big(f, v_h\big)_h\end{aligned}$$

for all $v_h \in W_{0,h}$.

(1b) Compute $u_h^k \in [V_{0,h} + u_{D,h}]$ such that

$$\big(d_t \widetilde{\varepsilon}(u_h^k), \widetilde{\varepsilon}(z_h)\big) = -\theta\big(\widetilde{\varepsilon}(u_h^k), \widetilde{\varepsilon}(z_h)\big)_h - \theta\big(\nabla w_h^k \otimes \nabla w_h^k, \widetilde{\varepsilon}(z_h)\big)_h$$

for all $z_h \in V_{0,h}$.

(2) Terminate the algorithm if $||d_t \widetilde{\varepsilon}(u_h^k)|| + ||d_t D_h^2 w_h^k|| \le \varepsilon_{\text{stop}} \min\{1, \tau_k\}$. Otherwise, define

$$\tau_{k+1} = \min\{2\tau_k, \tau_{\max}\},$$

set $k \to k + 1$ and continue with Step (1a).

For the following numerical experiments we use a maximum number of Newton iterations of $N = 5$, a maximum step size $\tau_{\max} = 10^5$, stopping tolerances $\varepsilon_{\text{Newton}} = 10^{-5}$, $\varepsilon_{\text{stop}} = 10^{-12}$ and $\alpha = 1$.

We analyse the performance of the iterative scheme by running the discrete algorithm for an initially flat configuration on a uniform grid of meshsize $h = 0.05$ and a prestrain parameter $\theta = 1000$. The left plot in Figure 2 shows the development of the energies $E_h^\theta(w_h^k, u_h^k)$ for the first fifty iterations $1 \le k \le 50$. We observe that the scheme effectively reduces the elastic energy. On the right-hand side of Figure 2 the automatically chosen step sizes are visualized. The adaptive time stepping scheme decreases the step size for the first iteration to $\tau_1 = 0.125$. The step sizes then gradually increase until they reach the maximum value $\tau_{\max} = 10^5$ after 23 iterations. Similar results were obtained for the parameter $\theta = 1$.

5.2. Controlled sphere-cylinder transition

The amount of prestrain specified by the parameter θ dictates the shape of minimizers for the elastic energy functional. In theory, minimizers approach spherical configurations as in the linearized von Kármán model for small values of θ. On the other hand, energy optimal configurations are expected to obtain cylindrical shapes as in the linearized Kirchhoff model for large values of θ. To investigate the various shapes an initially flat approximation of the unit disc $\Omega = B_1(0)$ is considered. It is defined by the initial configurations

$$u^0(x) = \begin{bmatrix} 0 \\ 0 \end{bmatrix}, \quad w^0(x) = 0, \quad x \in B_1(0).$$

We run the iterative scheme (Algorithm 5.1) for $\alpha = 1$ without applying any body force or boundary conditions, *i.e.*, we set $f = 0$, $\gamma_D = \emptyset$, and $u_D = 0$ and $w_D = 0$. To ensure uniqueness of discrete solutions an L^2-contribution is included in the discrete gradient flow. In particular, we define

$$(w_h, v_h)_{\text{ver}} = \big(D_h^2 w_h, D_h^2 v_h\big) + \big(w_h, v_h\big), \quad (u_h, z_h)_{\text{hor}} = \big(\widetilde{\varepsilon}(u_h), \widetilde{\varepsilon}(z_h)\big) + \big(u_h, z_h\big). \tag{5.1}$$

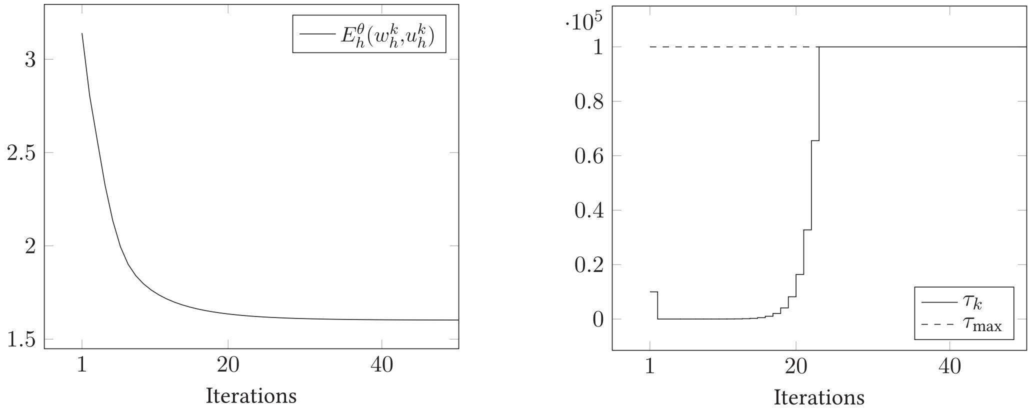

FIGURE 2. Energy development of the sequence $(w_h^k, u_h^k)_{k\geq 1}$ and step sizes $(\tau_k)_{k\geq 1}$ of the iterative scheme for the first fifty iterations with $\theta = 1000$ and $h = 0.05$.

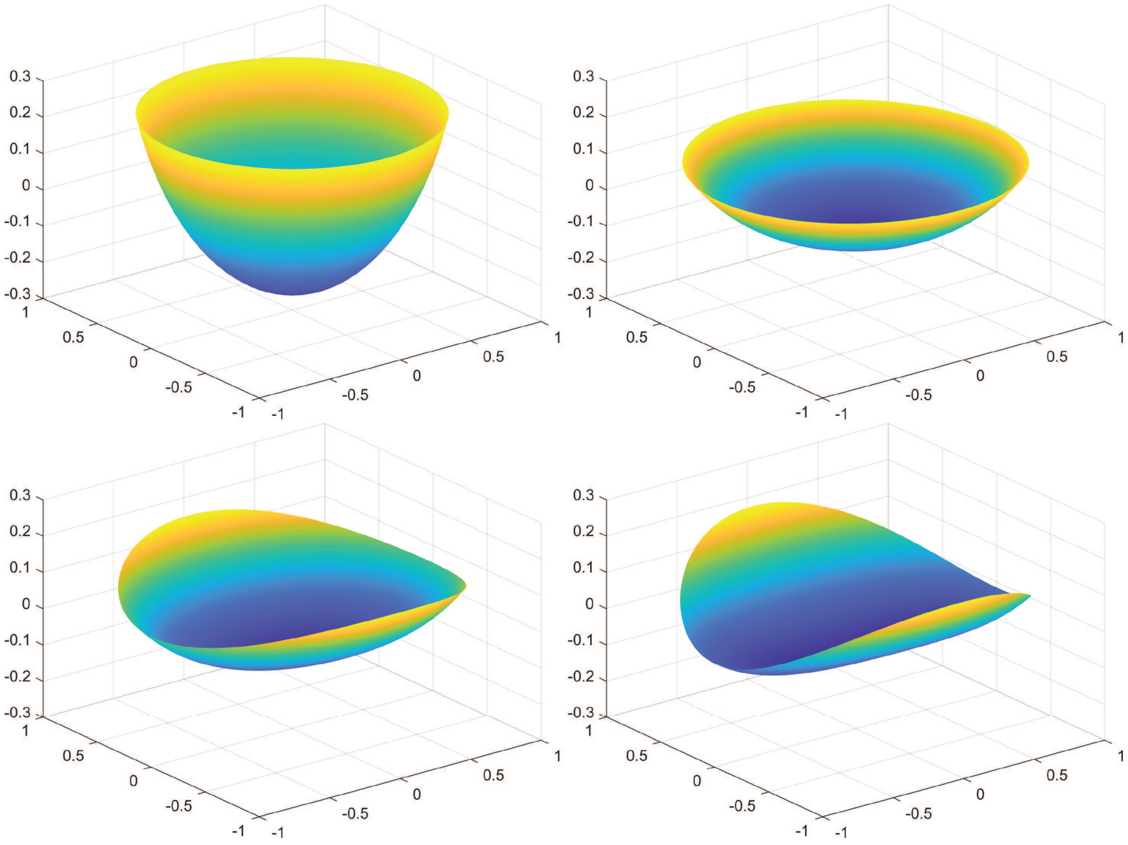

FIGURE 3. Numerical solutions of Algorithm 5.1 for an initially flat disk with $\theta = 1$ (*top left*), $\theta = 300$ (*top right*), $\theta = 350$ (*bottom left*) and $\theta = 1000$ (*bottom right*). The colors represent the vertical magnitude from dark (lowest) to bright (highest). A transition from spherical to cylindrical configurations for increasing values of θ can be observed.

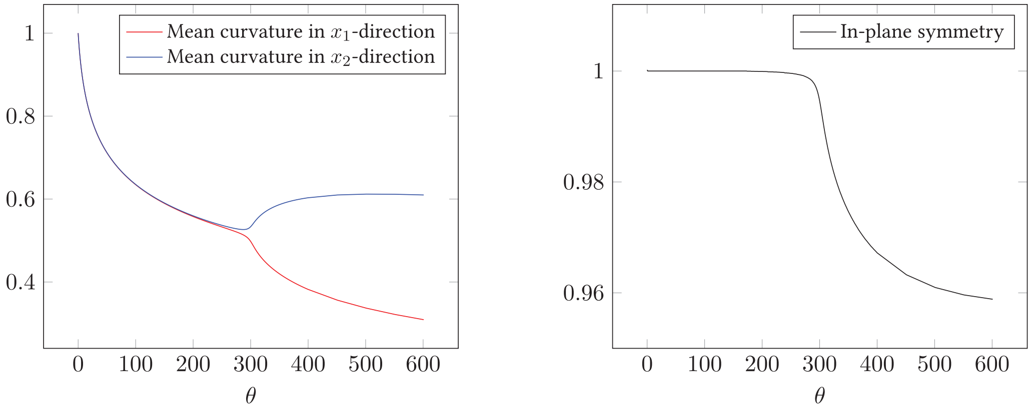

FIGURE 4. Development of the directional mean curvatures (*left*) and the quotient q_{sym}, see (5.2), of the directional in-plane deflections (right) of the final configurations for $\theta = 1, 2, \dots, 400$ and $\theta = 400, 450, \dots, 600$. A critical regime at around $\theta = 300$ appears from which on a stark break of symmetry occurs.

The corresponding numerical solutions for a grid of meshsize $h = 0.05$ and different values $\theta \in \{1, 300, 350, 1000\}$ are visualized in Figure 3.

As can be seen in Figure 3 we obtain a spherical shape for small values of θ which coincides with the theoretical conjectures. The configuration flattens as θ increases until some critical range of values $\theta \in [250, 350]$, at which a transition to a cylindrical shape takes place. The transformation occurs abruptly and sooner than theoretical observations might suggest, as minimizers of the Föppl–von Kármán model are known to approximate cylindrical minimizers of the linearized Kirchhoff model only in the limit $\theta \to \infty$.

So far we identified low-energy solutions of the discrete model for some fixed values θ. The remainder of this section is devoted to analyse the transition between the spherical and the cylindrical shape for intermediate values of the parameter θ. We aim at identifying some critical point θ_{crit} at which a drastic deviation takes place. Our previous experiments suggest that $\theta_{\text{crit}} \approx 300$. The graphs in Figure 4 display the directional mean curvatures and the quotient

$$q_{\text{sym}} = \frac{\max u_1 - \min u_1}{\max u_2 - \min u_2} \tag{5.2}$$

of the directional in-plane deflections of the final configurations for $\theta = 1, 2, \dots, 400$. The value q_{sym} quantifies symmetric properties of the in-plane deformation u, where larger deviations from the value one indicate more asymmetric, and in our case more cylindrical, states. We also include results using larger increments $\theta = 400, 450, \dots, 600$ to reduce the overall computation times.

We observe, that the directional curvatures remain nearly equal and the in-plane symmetry is almost constant for $\theta \lesssim 200$. For intermediate values $200 \lesssim \theta \lesssim 300$ slight deviations appear, whereas, for values greater than 300, the directional mean curvatures split apart and the symmetric properties decrease at a high rate. This is coherent with the observations from Figure 3, in which the spherical deformations flatten and stay symmetric at first but rapidly switch to a cylindrical shape at some point.

Similar experiments have been carried out in [10] with a different scaling of the elastic energy. In particular, the authors considered the energy $\widetilde{E}^\lambda$ defined by

$$\widetilde{E}^\lambda(u, w) = \frac{1}{24} \int_\Omega |D^2 w - I|^2 \, dx + \frac{\lambda}{8} \int_\Omega |\nabla w \otimes \nabla w + \widetilde{\varepsilon}(u)|^2 \, dx.$$

To draw a comparison between our experiments and their numerical results, we note that rescaling the elastic energy $\widetilde{E}^\lambda$ by a constant C (in this case $C = 12$) has no effect on its minimizers. Matching the parameters θ and λ of the membrane energies in E^γ and $\widetilde{E}^\lambda$, respectively, yields the relation $\theta = 3\lambda$. The critical value the authors achieved, at which the transition between spherical and cylindrical shape takes place, reads $\lambda_{\text{crit}} \approx 86$, hence $3\lambda_{\text{crit}} \approx 258$. It is difficult to quantify such a critical value in our numerical experiments since the transition is much smoother than the one observed in the first experiment of [10] for an initial flat configuration. However, the results observed therein suggest a very similar range of critical values. The developments of the directional mean curvatures and the symmetric properties agree with the results of the authors' second test in which an initial configuration with the shape of a potato chip is used instead.

5.3. Curvature inversion

The identity matrix I in the first part of the energy enforces a specific bending behaviour of energy optimal configurations. The strength of the prescribed curvature can be modified by scaling the matrix I by a factor $\alpha \in \mathbb{R}$. In particular, we consider the energy

$$E^\theta(u, w) = \frac{1}{2}\int_\Omega |D^2 w - \alpha I|^2 \,\mathrm{d}x + \frac{\theta}{2}\int_\Omega |\nabla w \otimes \nabla w + \widetilde{\varepsilon}(u)|^2 \,\mathrm{d}x$$

in which the forcing term is neglected. The sign of the factor α correlates to the sign of the specified surface curvature. The case $\alpha = 0$ is related to the corresponding singlelayer model which has been studied in [3]. We address in this section the inversion of the curvature which is modeled by letting $\alpha = 1$ go to $\alpha = -1$. Similar to the previous experiment neither an external force nor boundary conditions are applied, *i.e.*, $f = 0$ and $\gamma_D = \emptyset$, and we use $\Omega = (-1, 1)^2$. In addition to the L^2-contribution in the discrete gradient flow (5.1), we fix the vertical deflection of the midpoint $x_0 = [0, 0]^\mathsf{T}$ of the mesh to zero by prescribing $w(x_0) = 0$. Algorithm 5.1 is run with an initial flat configuration and $\alpha = 1$. Next, the parameter α is decreased by 0.05 and the algorithm is reapplied to the resulting configuration of the previous step. This process is repeated until $\alpha = -1$ is reached. Figure 5 shows the numerical solutions for $\theta \in \{0, 1000\}$ and $\alpha \in \{1, 0.7, 0.3, -1\}$. It is apparent from Figure 5 that for $\theta = 0$, for which $u_h = 0$ and only a linear system of equations has been solved to determine w_h, and any $\alpha \in [-1, 1]$ the strain density is distributed radially symmetric across the plate. The center always contains the least amount of strain while the values progressively increase towards the boundary of the object. When $\alpha = 0$ we obtain a completely flat configuration. For $\theta = 1000$ and $\alpha = 1$ the algorithm produces a cylindrical shaped object which is coherent with the observations of the previous experiments. For decreasing α the configurations flatten along paths with the largest directional curvature until all corner points of the plate reach an equal height for $\alpha \approx 0.3$. The numerical solutions then flatten evenly to a planar state for $\alpha \to 0$. In both cases $\theta \in \{0, 1000\}$ the processes are reversed for negative values of the parameter α with a change in the sign of the surface curvature.

5.4. Foldable cardboard

Next, we aim at analyzing the behavior of the bottom part of a deployed cardboard (compare with the right picture of Fig. 1), when the bistable mechanism is initiated by application of a force in a small radial area at the center of the plate. We consider a singlelayer plate, *i.e.*, $\alpha = 0$, whose vertical component w is clamped in a cylindrical shape *via* simple support boundary conditions on two opposing sides. No boundary conditions are enforced on the in-plane displacement u. The initial deformation is described by the data

$$u_D(x) = \begin{bmatrix} 0 \\ 0 \end{bmatrix}, \quad w_D(x) = -\frac{1}{2}\left(x_2^2 - 1\right), \quad x \in \Omega = (-1, 1)^2.$$

We set $\theta = 10^6$ and induce a gradually increasing vertical force, starting from $f = 0$ until the maximal value $f = -0.6 \cdot 10^6$ is reached, in the center $B_{1/10}(0)$ of the object. Algorithm 5.1 is applied to a regular cardboard without containing a crease line. The same experiment is carried out to a cardboard that is predamaged on a

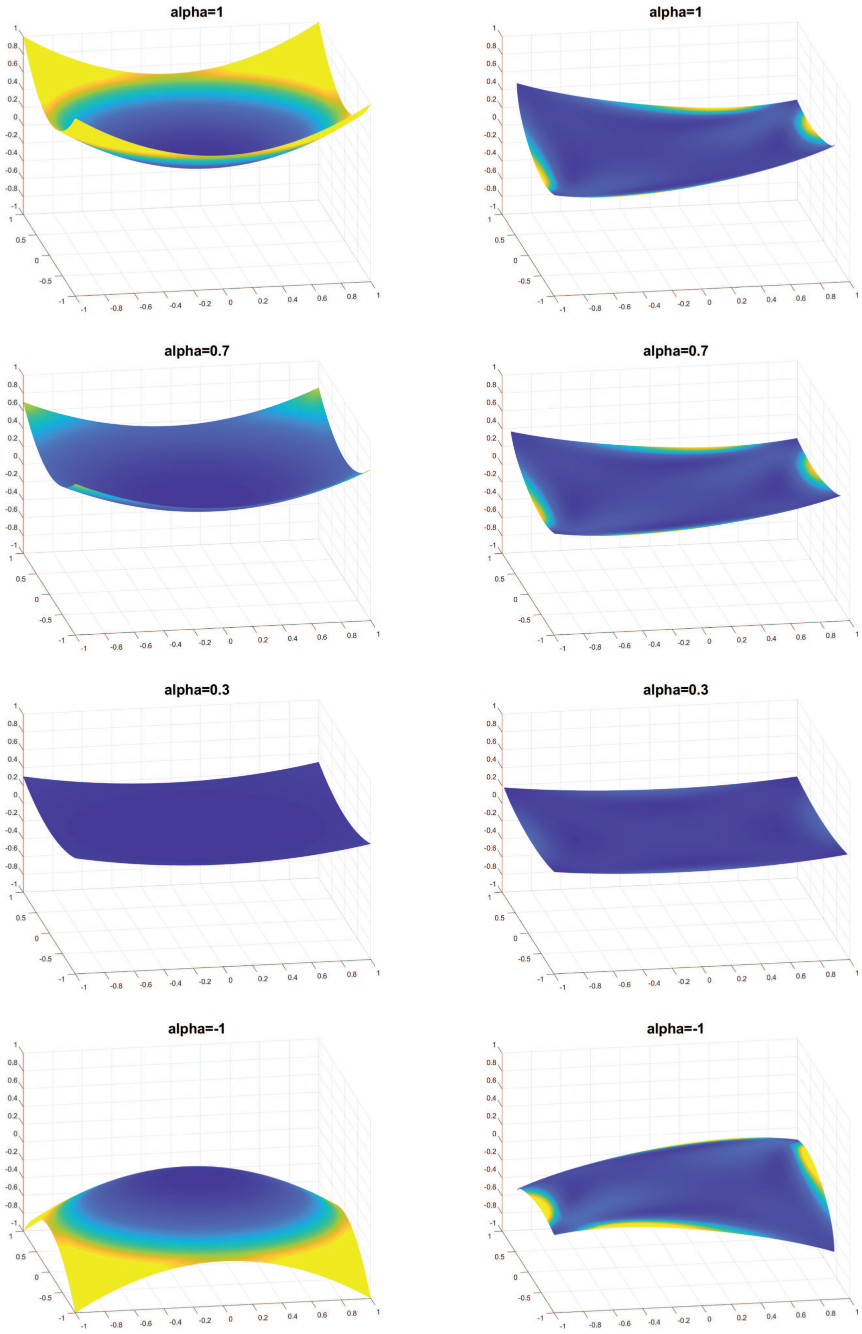

FIGURE 5. Numerical solutions of Algorithm 5.1 for $\alpha \in \{1, 0.7, 0.3, -1\}$ (*top* to *bottom*) with $\theta = 0$ (*left*) and $\theta = 1000$ (*right*). The colors represent the strain density from dark (lowest) to bright (highest). The transition from $\alpha = 1$ to $\alpha = -1$ induces a curvature inversion, where the value $\alpha = 0$ leads to flat configurations for arbitrary θ.

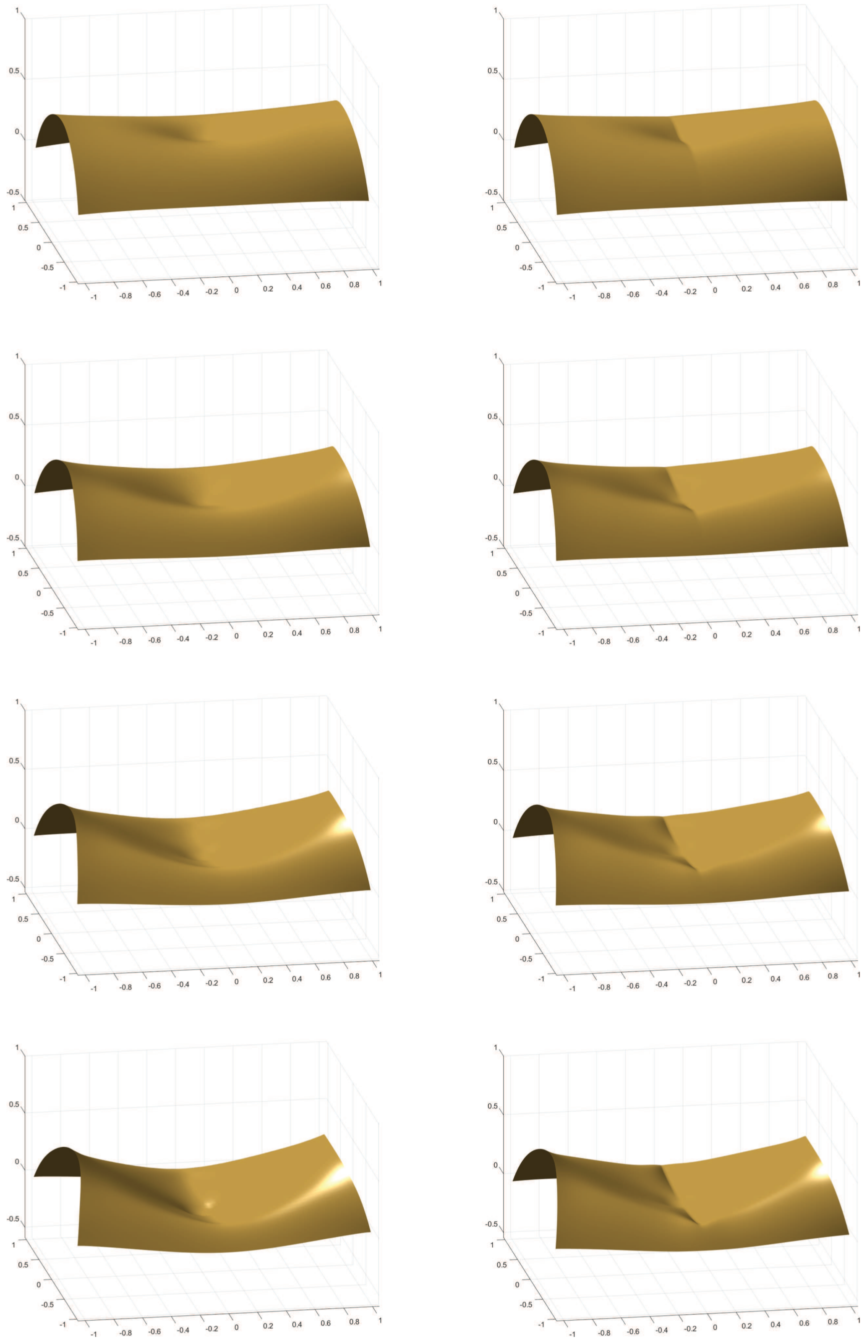

FIGURE 6. Numerical solutions for a cardboard without crease line (*left*) and with crease line (*right*) for a radial force acting in the plate center after 20, 30, 40 and 50 iterations of the algorithm. The deformation of the undamaged cardboard leads to an oval indentation profile whereas the predamaged cardboard obtains a rhombic indentation profile.

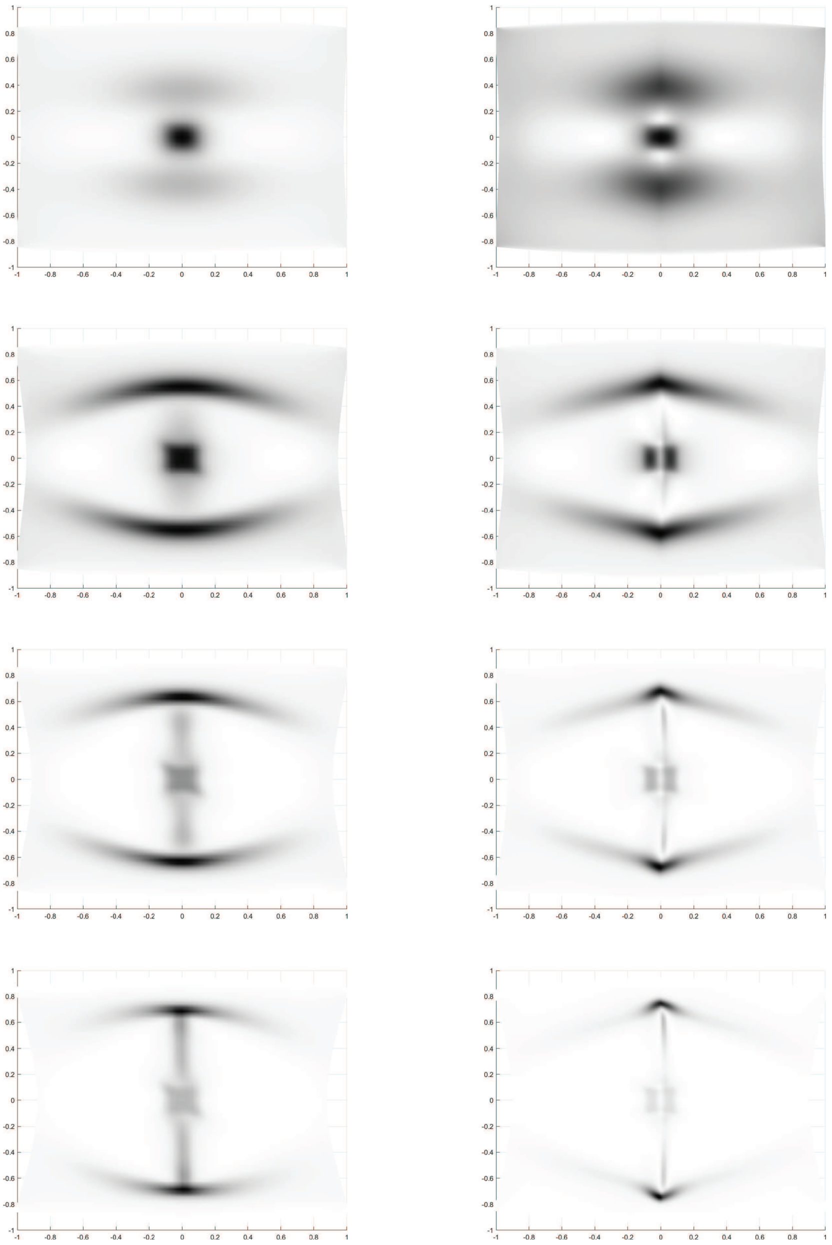

Figure 7. Top views of the numerical solutions for a cardboard without crease line (*left*) and with crease line (*right*) for a radial force acting in the plate center after 20, 30, 40 and 50 iterations of the algorithm with a shading of the bending energy densities $|D_h^2 w_h|$. In the undamaged cardboard a natural formation of a folding line across the plate center can be observed. In both the undamaged and predamaged models, lines of large curvature appear across the (formed) folding line close to the boundary of the plates. The distance between these creases and the boundary seems to match the crack length observed in the left picture of Figure 1.

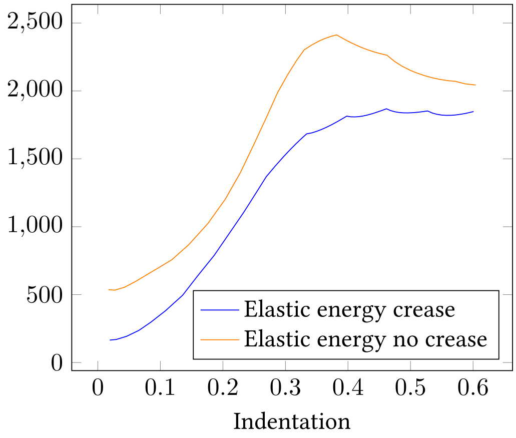

FIGURE 8. Energy development of the sequence $(w_h^k, u_h^k)_{k\geq 0}$ with and without crease line. In both cases we observe an energy barrier but the total elastic energy of the model with crease is persistently lower.

straight line $\mathcal{C} = \{0\}\times[-1,1]$ across its center. In the simulation this is achieved by assigning to nodes $z \in \mathcal{N}_h \cap \mathcal{C}_h$ on the crease line two seperate gradient values $\nabla w_1(z)$ and $\nabla w_2(z)$ corresponding to each side Ω_1, Ω_2 of the crease. This is equivalent to solving the discrete decoupled gradient flow separately on each subdomain subject to the continuity constraint $w_1(z) = w_2(z)$ for all $z \in \mathcal{N}_h \cap \mathcal{C}_h$. If DF_i and F_i denote the respective system matrices for the Newton scheme (Prop. 3.2) restricted to Ω_i, the continuity condition is enforced *via* Lagrange multipliers by solving the modified linear system of equations

$$\begin{bmatrix} DF_1 & 0 & I_1^\top \\ 0 & DF_2 & -I_2^\top \\ I_1 & -I_2 & 0 \end{bmatrix} \begin{bmatrix} \widetilde{w}_1 \\ \widetilde{w}_2 \\ \Lambda \end{bmatrix} = \begin{bmatrix} F_1 \\ F_2 \\ 0 \end{bmatrix}.$$

Here, $\widetilde{w}_i = w_i^k - w_i^{k-1}$ denotes the k-th update on each subdomain Ω_i containing the values $\widetilde{w}_i(z)$ and $\nabla\widetilde{w}_i(z)$ for all $z \in \mathcal{N}_h \cap \overline{\Omega}_i$, while the vector Λ includes the Lagrange multipliers. The matrices I_1, I_2 contain the values 0 or 1, encoding the condition $\widetilde{w}_1(z) = \widetilde{w}_2(z)$ for all $z \in \mathcal{N}_h \cap \mathcal{C}_h$. If the previous iterates w_1^{k-1} and w_2^{k-1} are continuous on $z \in \mathcal{N}_h \cap \mathcal{C}_h$ the condition guarantees the pointwise continuity $w_1^k(z) = w_2^k(z)$ of the next iterates for $z \in \mathcal{N}_h \cap \mathcal{C}_h$. Numerical solutions for the cardboard with and without crease line are visualized in Figure 6. The numerical simulations show that both plates are pushed downwards in the center. Initially, the cardboards are indented in a radially symmetric area. The indented area of the undamaged cardboard transforms to an oval shape and the natural formation of a crease line across the plate center can be observed. In the deformation profile of the predamaged cardboard a rhombic shape is visible instead. The indented areas are surrounded by lines of large curvature that emenate from the endpoints of the middle crease to the boundary of the plate. This is especially apparent from Figure 7 which contains top views of the numerical solutions shaded with respect to the elementwise bending energy densities. Figure 8 shows the developments of the total elastic energies of the respective numerical solutions in dependence of the indentation which is measured as the displacement at the center.

In both cases we observe an energy barrier between the unindented, cylindrical initial configuration and the indented configurations that contain large flat areas. The energy barrier of the plate without predamage is much larger due to an increased elastic resistance compared to the plate with crease. Interestingly, the distance of the wrinkles perpendicular to the formed line match the length of a crack that appeared in a real cardboard after repeated actuation, cf. Figure 1. This suggests a connection between the two phenomena.

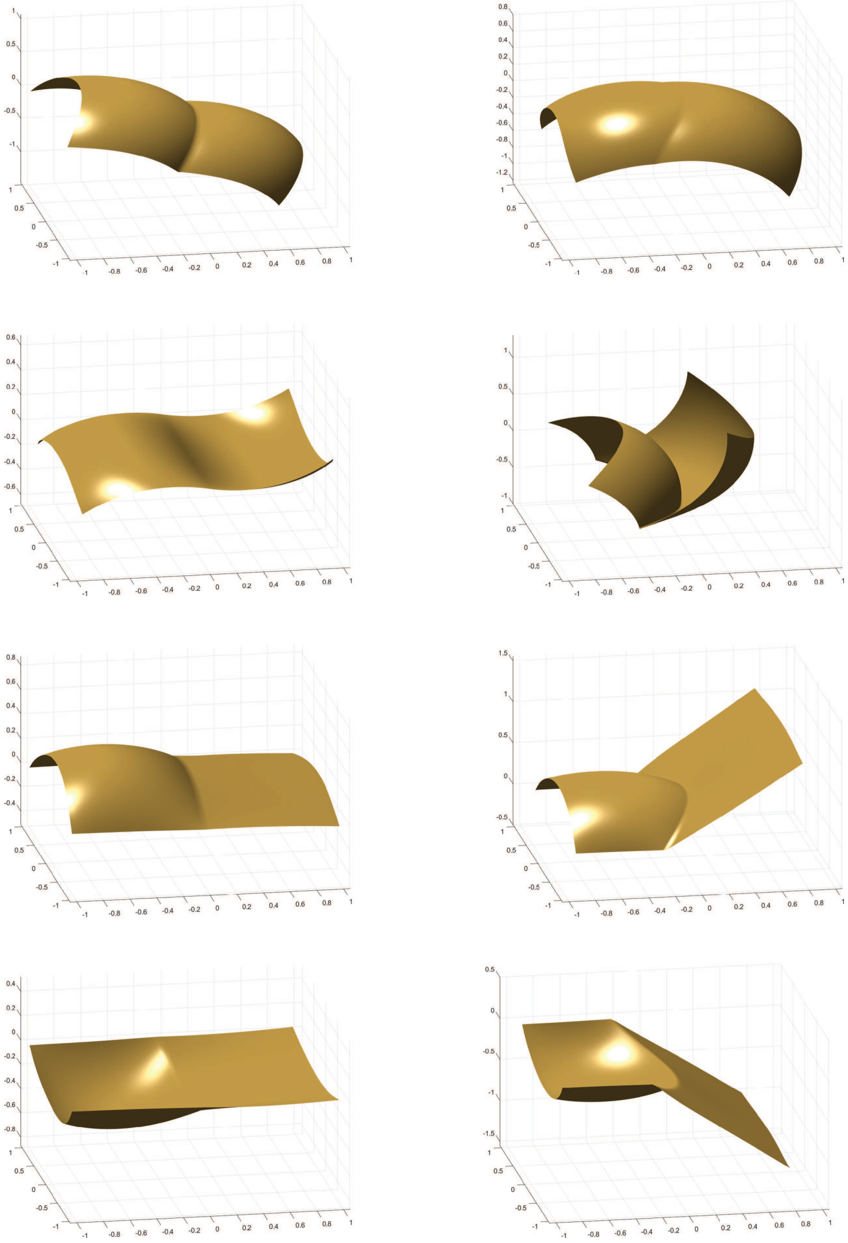

FIGURE 9. Visualization of the numerical solutions for $\alpha_1 = 1, 1, 1, -1$, $\alpha_2 = 1, -1, 0, 0$ (from *top* to *bottom*) combined with a straight (*left*) and a curved (*right*) crease. In the last two rows simple support boundary conditions are imposed along the upper and lower edge of the left subdomain. Drastic differences in the models with straight and curved crease geometries can be observed. For instance, the straight crease only leads to minor deflections of the right subdomain in the last two test, whereas the curved crease leads to significant deflections that appear in snapping mechanisms of Venus flytraps.

5.5. Bilayer plate folding

Finally, we combine elastic effects of bilayer plates with physical phenomena related to folding. The motivation stems from the fact that simulations of mechanisms like Venus flytraps *via* bilayer models are presumably more realistic than simulations obtained from singlelayer models which depend on the artificial application of boundary conditions or forcing terms. For instance, bilayer models are capable of describing swelling effects that enable the actuation of carnivorous plants. We give a brief overview over different configurations for various parameters $\alpha_1, \alpha_2 \in \mathbb{R}$ corresponding to the subdomains Ω_1, Ω_2 of $\Omega = (-1,1)^2$ when combined with different geometries of given crease curves $\mathcal{C}$ that separate the two regions. The discrete crease is either assumed to be a straight line $\mathcal{C}_h = \{0\} \times [-1,1]$ or a piecewise linear approximation of the arc

$$\mathcal{C}(t) = \left(\frac{1}{6}\sin(\pi t) + \frac{1}{3}, t\right), \quad t \in [-1,1].$$

Figure 9 contains numerical solutions for straight and piecewise linear crease geometries paired with various combinations of parameters $\alpha_1, \alpha_2 \in \{-1,0,1\}$ and $\theta = 1$. We observe drastic differences in the deformation profiles between the two crease geometries. Interestingly, the straight crease with $\alpha_1, \alpha_2 = 1$ leads to a kink while the curved crease leads to a nearly smooth deformation without significant jumps in the deflection gradient. In the last two tests a spontaneous curvature is only applied on the left part of the plate. The curved crease geometry leads to a snapping mechanism while the deflection on the right side remains nearly flat when a straight crease is included.

Acknowledgments

The authors acknowledge support by the DFG *via* the priority programme SPP 2256 *Variational Methods for Predicting Complex Phenomena in Engineering Structures and Materials* (441528968 and 441138507).

References

- [1] S. Bartels, Approximation of large bending isometries with discrete Kirchhoff triangles. *SIAM J. Numer. Anal.* **51** (2013) 516–525.
- [2] S. Bartels, Numerical Methods for Nonlinear Partial Differential Equations. *Springer Series in Computational Mathematics*. Vol. 47. Springer, Cham (2015).
- [3] S. Bartels, Numerical solution of a Föppl–von Kármán model. *SIAM J. Numer. Anal.* **55** (2017) 1505–1524.
- [4] S. Bartels, A. Bonito and R.H. Nochetto, Bilayer plates: model reduction, Γ-convergent finite element approximation, and discrete gradient flow. *Comm. Pure Appl. Math.* **70** (2017) 547–589.
- [5] S. Bartels, A. Bonito and P. Hornung, Modeling and simulation of thin sheet folding. *Interfaces Free Bound.* **24** (2022) 459–485.
- [6] A. Bonito, R.H. Nochetto and D. Ntogkas, Discontinuous Galerkin approach to large bending deformation of a bilayer plate with isometry constraint. *J. Comput. Phys.* **423** (2020) 109785.
- [7] D. Braess, Finite Elements, 3rd edition. Cambridge University Press, Cambridge (2007). Theory, fast solvers, and applications in elasticity theory. Translated from the German by Larry L. Schumaker.
- [8] J. Braun and B. Schmidt, An atomistic derivation of von-Kármán plate theory. *Netw. Heterog. Media* **17** (2022) 613–644.
- [9] P.G. Ciarlet, A justification of the von Kármán equations. *Arch. Ration. Mech. Anal.* **73** (1980) 349–389.
- [10] M. de Benito Delgado and B. Schmidt, Energy minimising configurations of pre-strained multilayers. *J. Elasticity* **140** (2020) 303–335.
- [11] M. de Benito Delgado and B. Schmidt, A hierarchy of multilayered plate models. *ESAIM Control Optim. Calc. Var.* **27** (2021) S16.
- [12] A.I. Egunov, J.G. Korvink and V.A. Luchnikov, Polydimethylsiloxane bilayer films with an embedded spontaneous curvature. *Soft Matter* **12** (2016) 45–52.

[13] M. Finot and S. Suresh, Small and large deformation of thick and thin-film multi-layers: effects of layer geometry, plasticity and compositional gradients. *J. Mech. Phys. Solids* **44** (1996) 683–721. Available from: `http://www.sciencedirect.com/science/article/pii/0022509696845480`.

[14] L.B. Freund, Substrate curvature due to thin film mismatch strain in the nonlinear deformation range. *J. Mech. Phys. Solids* **48** (2000) 1159–1174.

[15] G. Friesecke, R.D. James and S. Müller, A theorem on geometric rigidity and the derivation of nonlinear plate theory from three-dimensional elasticity. *Commun. Pure Appl. Math.* **55** (2002) 1461–1506.

[16] G. Friesecke, R.D. James and S. Müller, A hierarchy of plate models derived from nonlinear elasticity by Γ-convergence. *Arch. Ration. Mech. Anal.* **180** (2006) 183–236.

[17] K. Jonsson, Y. Ma, A.-L. Routier-Kierzkowska and R. Bhalerao, Multiple mechanisms behind plant bending. *Nat. Plants* **9** (2022) 1–9.

[18] C.S. Kim and S.J. Lombardo, Curvature and bifurcation of MgO–Al_2O_3 bilayer ceramic structures. *J. Ceram. Process. Res.* **9** (2008) 93–96.

[19] C. Lee, X. Wei, J.W. Kysar and J. Hone, Measurement of the elastic properties and intrinsic strength of monolayer graphene. *Science* **321** (2008) 385–388. Available from: `https://www.science.org/doi/abs/10.1126/science.1157996`.

[20] M. Lewicka and D. Lučić, Dimension reduction for thin films with transversally varying prestrain: oscillatory and nonoscillatory cases. *Comm. Pure Appl. Math.* **73** (2020) 1880–1932.

[21] M. Lewicka, L. Mahadevan and M.R. Pakzad, The Föppl–von Kármán equations for plates with incompatible strains. *Proc. R. Soc. London Ser. A. Math. Phys. Eng. Sci.* **467** (2011) 402–426.

[22] C.B. Masters and N.J. Salamon, Geometrically nonlinear stress-deflection relations for thin film/substrate systems. *Int. J. Eng. Sci.* **31** (1993) 915–925. Available from: `http://www.sciencedirect.com/science/article/pii/0020722593901032`.

[23] D. Padilla-Garza, Dimension reduction through gamma convergence for general prestrained thin elastic sheets. *Calc. Var. Part. Differ. Equ.* **61** (2022) 187.

[24] R. Sachse, A. Westermeier, M. Mylo, J. Nadasdi, M. Bischoff, T. Speck and S. Poppinga, Snapping mechanics of the venus flytrap (Dionaea muscipula). *Proc. Nat. Acad. Sci.* **117** (2020) 16035–16042.

[25] N.J. Salamon and C.B. Masters, Bifurcation in isotropic thinfilm/substrate plates. *Int. J. Solids Struct.* **32** (1995) 473–481. Available from: `http://www.sciencedirect.com/science/article/pii/002076839400129K`.

[26] M. Santilli and B. Schmidt, A Blake-Zisserman-Kirchhoff theory for plates with soft inclusions. *J. Math. Pures Appl.* **175** (2023) 143–180.

[27] B. Schmidt, Minimal energy configurations of strained multi-layers. *Calc. Var. Part. Differ. Equ.* **30** (2007) 477–497.

[28] B. Schmidt, Plate theory for stressed heterogeneous multilayers of finite bending energy. *J. Math. Pures Appl.* **88** (2007) 107–122.

[29] J.W. Suk, R.D. Piner, J. An and R.S. Ruoff, Mechanical properties of monolayer graphene oxide. *ACS Nano* **4** (2010) 6557–6564.

[30] Z. Zhang, K. Pei, H. Wu, M. Sun, H. Chai, H. Wu and S. Jiang, Bistable characteristics of hybrid composite laminates embedded with bimetallic strips. *Compos. Sci. Technol.* **212** (2021) 108880. Available from: `https://www.sciencedirect.com/science/article/pii/S0266353821002360`.